Title

Laser ablation induced vapor plume expansion into a background gas-Part B. Experimental Analysis

Authors

Wen, Sy-Bor
Mao, Xianglei
Greif, Ralph
et al.

Publication Date

2006-06-06

Laser ablation induced vapor plume expansion into a background gas – Part B. Experimental Analysis

Sy-Bor Wen[a)], Xianglei Mao [a)] , Ralph Greif [b)], Richard E. Russo [a)]

Abstract

Laser ablation of copper with a 4ns laser pulse at 1064 nm was studied with a series of synchronized shadowgraph (100 fs laser pulses at 400 nm) and emission images (spectral line at 515 nm). Data were obtained at two laser pulse energies (10, 30 mJ) and in three background gases (He, Ne, Ar) at atmospheric pressure. The laser energy conversion ratio and the amount of sample vaporized for ablation in each condition were obtained by the theoretical analysis reported in part A from trajectories of the external shockwave, internal shockwave, and contact surface between the Cu vapor and the background gas. All three quantities were measured from shadowgraph and emission images. The results showed that *E*, the amount of energy that is absorbed by the copper vapor, decreases as the atomic mass of the background gas increases; and *M*, the mass of the sample converted into vapor, is almost independent of the background gas [1]. A physical interpretation is given based on the phenomena observed in shadowgraph and emission images during the first tens of ns after the beginning of the laser pulse for ablation in different background gases.

In addition, an internal shockwave was observed in the emission images during the first tens of ns after the laser pulse, which strikes the surface and should be one of the mechanisms inducing the liquid sample ejection. Also, a significant vortex ring near the target was observed in emission images at longer times after the laser pulse (> 100 ns) which distorts the otherwise hemispherical expansion of the vapor plume.

---

a) Lawrence Berkeley National Laboratory, Berkeley, CA 94720

b) Department of Mechanical Engineering, University of California, Berkeley, California 94720

Keywords: Laser ablation, plasma shielding, shockwave, vortex ring

Introduction

Over the past several decades, researchers have utilized laser ablation for nano-material production, laser surgery, chemical analysis and numerous other applications. Most of these applications require precise control of the amount of sample mass removed and the region affected by the laser energy. A better understanding of laser ablation is required to optimize these applications.

The amount of the sample vaporized, *M*, and the amount of laser energy converted to the vapor plume, *E*, are functions of laser wavelength, laser energy, type of background gas, and background gas pressure [2]. Fast-time resolved shadowgraph [3] and emission images are two experimental methods which are able to record the evolution of the vapor plume and shockwaves up to ns scale. Shadowgraph images allow the direct measurement of the propagation of different compressed waves during and after the laser pulse generated by the rapidly expanding vapor plume; emission images are capable of monitoring the evolution of the vapor plume and the migration of the higher emission region within the vapor plume. By inspecting a series of fine-time resolved shadowgraph and emission images from the beginning of the laser pulse, possible mechanisms which determine the magnitude of E and M for ablation in different conditions are obtained.

In this work, the phenomena that occur during nanosecond laser ablation were studied with a series of synchronized fast-time resolution shadowgraph and emission images (the segment for each image is 1ns during the first 30ns and 1 to 5ns after that) for different background gases (He, Ne and Ar) and laser energies (10 and 30mJ). An external shockwave, laser supported detonation wave (LSD) and laser supported combustion wave

(LSC) [4] are observed in shadowgraph images. In addition, liquid ejection from the sample surface and the spatial variation of the absorption coefficient (which is a function of free electron number density) can be observed in the shadowgraph images during the first tens of ns from the beginning of the laser pulse. Evolution of the internal shockwave in the vapor plume and the size variation of the vapor plume during ablation are observed in the emission images. In conjunction with a previous theoretical analysis [5], the measurements of trajectories of the internal and external shockwaves, and the size evolution of the vapor plume provide the value of the laser energy conversion efficiency, E_{plasma} / E_{laser}, and the mass of the sample vaporized, M, for different background gases and laser energies.

The variation of E_{plasma} / E_{laser} is attributed to plasma shielding which occurs when laser energy passes through the highly ionized vapor plume and the compressed background gas behind the external shockwave. A laser supported detonation wave (LSD) and a laser supported combustion wave (LSC) which occur during the first tens of ns are consequences of plasma shielding [3]. The constant value of M for ablation in different background gases is related to the result that the starting time of the plasma shielding is almost the same for the different background gases. The major evaporation stops when plasma shielding, which blocks the laser energy from reaching the sample surface, occurs.

In addition to a detailed study of the dynamics of the vapor plume expansion during ns laser ablation, the present work provides an experimental foundation for our theoretical analysis [5]. An internal shockwave is recorded in emission images, which was predicted in the analysis. Liquid sample ejection shows a strong correlation with the

interaction of the internal shockwave with the sample as determined from the shadowgraph and emission images. The measured shape of the external shockwave, vapor plume and internal shockwave (before the second interaction with the sample surface) were close to hemispherical which is a basic assumption in the theoretical analysis [5]. Deviations between experimental data and the theoretical analysis [5] are attributed to the presence of a vortex ring [6] near the sample surfac which was not included in the theoretical analysis. The vortex ring provides an additional forward motion of the expanding vapor plume.

Experiment

A diagram of the experimental system is shown in Figure 1. A Nd:YAG laser (New Wave Research, Minilase II), operating at 1064 nm with a 4-ns pulse duration, was used as the ablation source. This laser beam was focused using a quartz lens onto a pure copper sample ($2 \times 20 \times 20 mm$) to a spot diameter of ~300 μm. Two sample orientations with respect to the ablation laser were used. For high resolution shadowgraph and plume emission imaging from 0 to 30ns after the start of the laser pulse, the thickness of the sample (2 mm) was facing the incoming laser beam. This geometry reduces interference fringes of the probe beam at the boundary of the sample and increases the resolution of the images. However, the diameters of the external shockwave front and vapor plume become larger than this dimension ~50ns after the laser pulse. Laser ablation on the short edge of the sample can no longer be approximated by the ablation on a semi-infinite surface, which makes analysis of the laser ablation process more complicated. For longer times after the laser pulse (>~30ns), the shadowgraph and plume emission images were measured with the larger face ($20 mm \times 20 mm$) of the sample facing the ablation laser. We verified that the measured external shockwave and the vapor plume were almost the same size for both orientations 30ns after the laser pulse.

A Ti: sapphire laser (Spectra-Physics, TSA) with a 100-fs pulse duration was used as the probe beam for the shadowgraph images. The 800 nm beam passed through a potassium dihydrogen phosphate (KDP) crystal, forming a probe beam at 400 nm that was directed perpendicular to the ablation laser beam. The probe beam was directed to a CCD camera (NIKON D70) after passing through a narrowband 400 nm filter. The time delay between the fs probe and ns ablation beams was controlled using a delay generator

(Stanford Research, DG 535). The actual delay time was measured using photodiodes in each optical path with an oscilloscope (Tektronix DSA 602A).

For spectral emission measurements in the vapor plume, the plasma was imaged onto an intensified Charge-Coupled Device (ICCD) with 1024×1024 pixels (Princeton Instruments, PI MAX 1024 Gen II) through a camera lens. A narrow band filter at 515nm was inserted between the camera lens and the ICCD to exclude all line emission from argon, neon, helium and copper, except for the 515.32nm emission line of copper. The emission and shadowgraph imaging systems were aligned in the same plane but perpendicular to each other. Both the emission and shadowgraph images could be recorded at the same time after the ablation laser pulse.

The crater volumes were measured using a white-light interferometric microscope (New View 200, Zygo). The down volume, defined as the volume below a reference surface, and the upper volume, defined as the volume above the reference surface, were measured after 200 pulses, for each experimental condition. The reference surface was the unablated sample. The ablated sample surfaces were washed with methanol before measuring the crater volumes.

The experiments were conducted under three different background gases (helium, neon, and argon) with a pressure of 1atm and flow at ~3L/min, and at two laser energies (10 and 30 mJ).

Results and Discussion

The measured external shockwave positions and the size of the vapor plume for ablation of a copper sample in different background gases (argon, helium, and neon) are

shown in Fig. 4-9; simulated values for the size of the vapor plume and the positions of internal and external shockwaves are also shown in the same figures. The detailed analyses of the propagation of the external and internal shockwaves, and the size evolution of the vapor plume were presented in Ref. 5. The total laser energy E converted to thermal and kinetic energies [7] of the vapor plume (vaporized sample) and to the background gas, and the mass M of the vaporized sample were determined by changing the E and M values specified in the analyses until the best fitting of experimental data with the numerical simulations was obtained. The ratio E/E_{laser} for ablation in helium, ~70-80%, was much larger than that in argon, ~30-35%, and in neon, ~35-40%. However, for the same incident laser energy (E_{laser}), the vaporized mass in the three gases was almost equal. These data are consistent with the measured crater volumes for ablation in the three background gases (cf. table 1); when the incident laser energy was the same; the measured down volumes (cf. Fig. 10) of the craters agreed to within 5% for ablation in all three background gases.

Physical phenomena observed during and after the laser pulse in the shadowgraph and emission images along with their possible explanations are listed below in the time sequence in which they occur (c.f. Fig. 11). The start time and the occurrence of these phenomena are associated with the laser energy conversion ratio, the amount of the mass that is vaporized, and the propagation of both the vapor plume and shockwaves.

1. The laser material interaction during the first time interval (from the start of the laser pulse to when the electron number density reaches the critical number density; approximately 2ns, , Fig. 11 and 12)

The laser material interaction during the laser pulse can be divided into two time intervals

based on the time when the vapor plume reaches the critical number density n_{ec} [8,9] (c.f. Fig. 12).

$$n_{ec} = m_e \varepsilon_0 \omega^2 / e^2$$

The first interval starts from the beginning of the laser pulse to when the electron number density reaches the critical number density; the second interval is from the end of the first interval to when the laser pulse stops. For both time intervals, the first order approximation of the evaporation process of the sample can be determined from the solution of the following equations:

The energy conservation equation in the sample [10]

$$\rho c_p(T) \frac{\partial T}{\partial t} = \frac{\partial}{\partial z}\left(K(T) \frac{\partial T}{\partial z} \right) + Q_{ab,laser}(z,t) \qquad (3.1)$$

The Hertz-Knudsen formula for the net evaporation rate is [4]

$$v_0 = s \frac{p_s(T_s) - p_0}{\rho_0 \sqrt{2\pi k_B T_s / m}}, \quad (3.2)$$

The mass, momentum, and energy conservation equations in the vapor phase [11]

$$\frac{\partial \rho}{\partial t} + \nabla \cdot (\rho \vec{V}) = 0 \quad (3.3)$$

$$\rho \frac{\partial \vec{V}}{\partial t} + \rho(\vec{V} \cdot \nabla)\vec{V} = -\nabla p \quad (3.4)$$

$$\rho \frac{\partial (c_p T)}{\partial t} + \rho(\nabla c_p T)\vec{V} = -p \nabla \cdot \vec{V} + Q_{ab,v,laser} \qquad (3.5)$$

The electron generation equation [12]

$$\frac{dn_e}{dt} = \left(\frac{dn_e}{dt} \right)_{photoionization} + \eta_{casc} n_e - \eta_{diff} n_e - \eta_{rec} n_e^{\,2} \quad (3.6)$$

The first two terms are electron generation by photoionization and cascade ionization; the last two terms are electron depletion by diffusion and recombination.

Since the electron number density is lower than the critical electron number density during this first time interval, most of the laser energy reaches the sample surface and supports the evaporation process. Therefore, the energy source term, $Q_{ab,laser}$, in Eq. (3.1) is only weakly affected by the presence of the vapor plume, and can be specified by the laser parameters and the optical properties of the sample. Initially when the laser radiation arrives at the sample, the pressure above the sample surface, p_0, which affects the laser-material interaction and the subsequent amount of the sample mass vaporized, is equal to the ambient gas pressure (1atm in the present experiments, cf. Eq. (3.2)); The density of the vapor plume ρ_0, however, is not necessarily the same as the density of the background gas. Shortly after the start of significant evaporation, a rapidly expanding vapor plume appears which covers the laser spot. The pressure above the sample, p_b, is equal to the pressure at the bottom of the vapor plume, which can be approximated by a free expansion relation. Therefore, the expansion is almost independent of the background gas properties within a few ns after the time when the vapor plume appears [2,13]. During the first time interval, only the vapor plume pressure (which inhibits sample evaporation and is equal to the background gas pressure initially) and not the background gas density (since the inertia of the background gas is not important during the early time) shows significant effects on the laser-material interaction. The laser energy conversion efficiency, the temperature field of the sample with the subsequent melting layer thickness, and the amount of sample vaporized are almost independent of the mass density of background gas but do depend on the background gas pressure during this time interval. Therefore, the laser energy conversion efficiency, the amount of the sample mass vaporized, and the melting layer thickness are almost the same for different

background gases during this time interval as long as the gas pressure is the same.

2. The laser-material interaction during the second time interval (from when the electron number density is larger than the critical number density to when the laser pulse ends, Fig. 11 and 12)

The temperature and the accompanying electron number density of the vapor plume continue to increase during the evaporation process by absorbing the incoming laser energy. Once the electron number density is greater than the critical number, the electrons generate new electrons by impact ionization of the atoms in the vapor. A cascade growth of the electron density occurs within the vapor plume; i.e. avalanche ionization [14]. Most of the remaining laser energy then is absorbed in the vapor plume by inverse Bremsstrahlung and photoionization. The high electron number density results in strong reflection at the contact surface and strong absorption in the vapor plume, blocking the incoming laser energy from reaching and heating the sample surface. Consequently, little laser energy reaches the sample surface and the amount of sample vaporized during the second time interval is much smaller than that of the first time interval.

The time when the second stage starts depends on how fast the vapor plume researches the critical electron number density. The evolution of the electron number density of the vapor plume depends on the temperature and mass density of the vapor plume. Both of these quantities depend on the evaporation speed of the sample and the dynamics of the expansion of the vapor plume during the first stage, which are almost independent of the atomic mass but depends on the pressure of the background gas as discussed in the last section.

Once the electron density of the vapor plume is greater than the critical density, the vapor

plume is effectively heated by absorbing the incoming laser energy which significantly accelerates its expansion speed. The rapidly expanding vapor plume further compresses the background gas as it expands, which generates a strong external shockwave in the background gas region, with a similar speed to that of the high temperature vapor plume (cf. figs. 4-9). Once the highly expanding external shockwave is generated, the compressed background gas behind the external shockwave also is highly ionized , and can reflect the incoming laser energy. The laser energy conversion ratio depends on the reflection and absorption coefficients of both the vapor plume and the compressed background gas. Both quantities are functions of the electron number densities, and are determined by the expansion speed of the vapor plume and the external shockwave; both are strongly affected by the atomic mass of the background gas.

3. Major sample melting and evaporation (during the first time interval of the laser-material interaction, Fig. 11)

Based on the discussion of the previous two sections, the primary melting and evaporation of the sample occurs during the first stage of the laser-material interaction when the electron number density of the vapor plume is less than the critical value. Also as mentioned in the last section, the melting and evaporation rates of the sample and the time duration of the first stage of the laser-material interaction depend on the background gas pressure but not on the type of the background gas. Therefore, the melting layer thickness and the amount of sample vaporized should be the same for the ablation in different background gases for the same pressure and laser energy as in the present study. This is in agreement with the amount of sample vaporized that was measured in the present study for ablation in the three different background gases (He, Ne, Ar) with

different laser energies (10 and 30mJ).

4. Plasma shielding with a laser supported detonation wave (LSD) (during the second time interval of the laser-material interaction) and a laser supported combustion wave (LSC) [4,14](from a few to tens of ns after the laser pulse, Fig. 11, 13 and 24)

The speeds of the external shockwave and the vapor plume are similar (cf. figs. 4-9) at the beginning of the second time interval, and are close to the free expansion speed of the vapor plume. The free expansion speed is determined by E_{vapor} and M only. E_{vapor} at the beginning of the second time interval is the energy transferred from the laser to thermal and kinetic energy of the vapor plume during the first time interval, which is almost independent of the type of the background gas (as discussed in part 1). Therefore, the external shockwave speed is almost the same in the three background gases during the first few ns. Since the atomic mass of Ar is double that of Ne and 10 times larger than He, the sound speed in Ar is about 1.4 times less than Ne and 3.2 times less than He. Therefore, the Mach number along with the temperature (Eq. 3.7) behind the external shockwave for ablation in Ar is about double that in Ne and 10 times larger than that in He [15].

The compressed background gas layer behind the rapidly expanding external shockwave is ionized. The electron density within this region is determined from the temperature and the ionization potential of the gas as $n_e \propto e^{-E_{ion}/kT}$.

The temperature of the compressed background gas region can be approximated by a uniform temperature with the value obtained from the jump condition behind the shockwave [16] ; i. e.

$$\frac{T_e}{T_g} = 1 + \frac{2(\gamma_g - 1)}{(\gamma_g + 1)^2} \frac{\gamma_g M_e^{\ 2} + 1}{M_e^{\ 2}} (M_e^{\ 2} - 1) \qquad (3.7)$$

The Mach number in the three background gases are $M_e(Ar) > M_e(Ne) > M_e(He)$ as discussed previously; the temperature of the compressed background layer are $T_e(Ar) > T_e(Ne) > T_e(He)$, The ionization potentials of the three background gases are 24.6eV (He) > 21.6eV (Ne) > 15.8eV (Ar); the electron density of the compressed gas behind the external shockwave for ablation in argon is much larger than in neon or helium during the first few ns from the beginning of laser ablation.

For ablation in argon, the electron number density of the compressed background gas layer is high enough to absorb most of the incoming laser energy and generate a self-sustained laser supported detonation wave (LSD). The LSD moves faster than the external shockwave and propagates toward the laser source (c.f. Fig. 13). In argon for both E=10 and 30mJ, this LSD can be observed from 4 - ~9ns after the laser energy reaches the sample. For neon, only for E=30mJ can a weak LSD be observed between 4 to 7ns after the laser energy reaches the target. In helium, no LSD was observed for both E=10 and 30mJ.

The propagation speed of the LSD is proportional to the laser fluence, and is approximated by [17]

$$U = \left[2(\gamma_g^{\ 2} - 1) I_{laser} / \rho_g \right]^{1/3} \quad (3.8)$$

Here I_{laser} is the laser fluence which is assumed to be fully absorbed and used in supporting the LSD. The propagation of the LSD was measured for two different spot sizes, $d \approx 210$ and $\approx 300 \mu m$ in argon with E=30mJ. The laser fluence for $d \approx 210 \mu m$ was about twice that for $d \approx 300 \mu m$, and the LSD distance measured from

the tip of the vapor plume (cf. figure 13) for $d \approx 210\mu m$ was about 2.4 times larger than that for $d \approx 300\mu m$. This ratio is higher than the value that is estimated from Eq. (3.8), which is 2. The difference between the experimental ratio and that predicted by Eq. (3.8) is due to the changes in the laser energy coupling efficiency in the LSD for different expansion speeds (different size laser spots), which is not considered in Eq. (3.8).

After the detonation wave has been formed, most of the laser energy is absorbed within a small distance behind the LSD front. The high electron density region can also can be observed in the shadowgraph images (Figs. 14-19), which correspond to the dark region behind the detonation wave front.

The LSD stops propagating at a time when the laser energy is below a threshold value [18] which is ~7ns in the present study. From ~10 to ~30ns after the laser pulse, however, the central tip of the vapor plume continues to move faster than other parts of the vapor plume and forms an additional bump at the top the hemispherical vapor plume (c.f. Fig. 14-19). This additional protuberance was observed for all background gases and the laser energies used in these experiments. The occurrence of this protuberance is likely due to nonuniform heating within the vapor plume as the laser passes through it; more laser energy is absorbed at the top of the vapor plume. Consequently, both the temperature and pressure are higher near the top of the vapor plume compared to other regions during and after the laser pulse, which propels the adjacent external shockwave at a faster rate away from the sample when compared to the regions far from the tip. This mechanism is similar to that of the laser supported combustion wave (LSC) which occurs at lower laser fluence [19].

4. Converting laser energy to the gas in the ablation system (during the second time

interval of the laser material interaction, Fig. 12)

Reflection of the incident laser energy occurs at the front edges of the three possible high electron density regions: the vapor plume, the compressed background gas behind the external shockwave and the laser supported detonation wave (LSD). Because of the negligible electron diffusion between each region during the time interval when the laser is on, a significant portion of the laser energy is reflected from the above interfaces and may not be absorbed by the vapor plume, which reduces the laser energy conversion efficiency. The reflection coefficient of the plasma is obtained from Fresnel's law [20]:

$$R(\omega) = \left| \frac{\sqrt{\varepsilon(\omega)} - 1}{\sqrt{\varepsilon(\omega)} + 1} \right|^2 \qquad (3.8)$$

The dielectric function, $\varepsilon(\omega)$, can be obtained from the Drude formula [19]:

$$\varepsilon_{dr}(\omega) = 1 - \frac{{\omega_p}^2}{\omega(\omega + i\upsilon_c)} \qquad (3.9)$$

where υ_c is the collision frequency and ω_p is the plasma frequency given by

$$\omega_p = \left(\frac{e^2 n_e}{\varepsilon_0 m} \right)^{1/2} \qquad (3.10)$$

In helium, the higher sound speed results in a lower Mach number of the external shockwave and the lower temperature of the compressed background gas layer as discussed in part 3. With the lower temperature of the compressed background gas , higher ionization potential, and a maximum of only two free electrons being produced during ionization, the electron density behind the external shockwave for ablation in helium is much less than that in neon and argon for the same laser energy. From the above relations, the lower electron number density corresponds to a smaller reflection

coefficient at the front surface of the external shockwave. In addition, with the LSD and the associated high electron density region being absent for ablation in helium, the reflection of the incoming laser is further reduced. Therefore, for laser ablation in helium, more laser energy can reach the vapor plume without being reflected at the plasma boundary. The higher expansion speed of the vapor plume for ablation in helium also reduces the electron density and the consequent absorption coefficient within the vapor plume during the second time interval. However, since the absorption coefficient of the vapor plume for the IR laser is very large, $>\sim 1\times 10^{4} m^{-1}$ for inverse Bremsstrahlung absorption only [9], most of the laser energy will be absorbed by the vapor plume after passing through the compressed background gas region for ablation in all three different background gases.

The total laser energy absorbed by the vapor plume is not only affected by the absorption coefficient of the vapor plume, but also by the size of the vapor plume. Since the vapor plume undergoes an almost 1D expansion in the first few ns after the laser energy reaches the sample surface, the temperature and density are inversely proportional to the size of the vapor plume. Assuming the ionization ratio in this temperature range is almost constant, the electron density is also almost inversely proportional to the size of the vapor plume. The optical path is linearly proportion to the vapor plume size for the 1D expansion. Thus, the optical depth, which is the product of the absorption coefficient and the optical path, is independent of which background gas was present. The background gas affects the amount of the laser energy absorbed by the vapor plume by changing the reflectivity of the interface between the compressed background gas and the ambient gas. Since less laser energy will be reflected for ablation in a low atomic mass and a high ionization potential background gas, higher laser energy conversion efficiency is

achieved for ablation in helium than in argon.

5. Propagation of the external shockwave (from the end of the laser pulse until ~1μs, Fig. 11 and 14-19)

The external shockwave strengthens and can be observed in the shadowgraph images after ~3ns (cf. fig.14-19), when the vapor plume reaches the critical value and significant plasma shielding causes the vapor plume to expand faster. Since the laser spot size (~300μm) is not infinitesimal, the external shockwave changes from 1D to 3D propagation during the first few ns. The propagation speed of the external shockwave and the free expansion speed of the vapor plume are similar during this time. From 10's to ~100ns, the propagation of the external shockwave can be approximated by the relation, $r_{ext} = C_1(E_{ext}/\rho_g)^{1/5} t^{2/5}$, according to the approximate study for a strong explosion proposed by Chernyi [21]. Although this relation happens to be the same as Sedov's law [22], the density, pressure, and temperature distributions predicted using Sedov's law from the center to the edge of the external shockwave cannot be used to obtain the density, pressure, and temperature distributions within the vapor plume. The deviation of true laser ablation from Sedov's law is due to the presence of the vapor plume inside the external shockwave region, which is not consistent with the condition considered in Sedov's law (a blast wave generated by a point energy release). The speed of the external shockwave decays to a sound wave as the time after the laser pulse increases and the pressure behind the external shockwave approaches the background gas pressure. A few μs after the laser pulse, the pressure of the vapor plume is almost the same as the background gas pressure.

The simulated trajectories of the external shockwave fit very well with the experimental data in all experimental conditions even though the simulated trajectories of the contact surface do not provide good agreement with experiments ~100's ns after laser pulse, for ablation in helium and/or with higher laser energy (30mJ). The good agreement results from the increase in the separation between the external shockwave and the contact surface ~100ns after the laser pulse (cf. Figs. 4-9). After ~100ns, the propagation of contact surface has little effect on the propagation of the external shockwave.

6. Internal shockwave (from the end of the laser pulse until ~100ns, , Fig. 11 and 20-23)
When the vapor plume expands supersonically, an internal shockwave is formed in the vapor plume to balance the velocity and high backpressure generated by the external shockwave. This internal shockwave reflects back and forth within the vapor plume until the vapor plume expansion slows. The propagation of the internal shockwave can be seen in the line emission images (Fig.20-23), where a high emission portion of the vapor plume moves back and forth inside the vapor plume. From both our current simulation and experimental data, only two internal shockwave reflections can be observed. The first time the internal shockwave strikes the target is at ~10 ns after the end of the laser pulse. The second time the internal shockwave strikes the sample surface is about ~100 ns. These times depend on the specific background gas and the laser energy. During the first internal shockwave sample interaction, the internal shockwave maintains a nearly hemispherical shape when approaching and when leaving the sample. During the second internal shockwave sample interaction, the internal shockwave remains almost hemispherical until coming close to the sample; then the hemispherically shaped internal shockwave front begins to distort. The internal shockwave front changes to a funnel

shape when it strikes the sample due to the presence of a vortex ring near the sample. When the internal shockwave approaches the vortex ring, the additional outward velocity provided by the vortex ring retards the propagation of the internal shockwave toward the sample. Since the central part of the internal shockwave is less affected by the vortex ring, the internal shockwave changes from a convex shape to a concave shape. Hence, during the second reflection, the shape of the internal shockwave is no longer hemispherical as it approaches the sample. The Mach number of the reflected shockwave, M_R, is related to the Mach number of the incident shockwave, M_S, according to [14]

$$\frac{M_R}{M_R{}^2-1}=\frac{M_S}{M_S{}^2-1}\sqrt{1+\frac{2(\gamma_v-1)}{(\gamma_v+1)^2}(M_s{}^2-1)\left(\gamma_v+\frac{1}{M_s{}^2}\right)}$$

where γ_v is the specific heat ratio of the vapor plume, which is $5/3$ in our experiments. The maximum possible value of M_R (with $M_S \to \infty$) is $M_R = 2.236$. Thus, the strength of the shockwave is reduced significantly after each reflection and may be the reason why there are only two internal shockwave reflections observed in our experiments.

7. Melted sample ejection (a few ns after the end of the laser pulse, Fig. 11, 13, and 24)
When the internal shockwave strikes the sample surface, liquid metal can be ejected (Richtmeyer-Meshkov instability [23]) since a large amount of momentum is transferred to the sample (Fig. 24a). A rim around the crater can be generated when the melted region is pushed outward from the crater due to the interaction between the internal shockwave and the liquid. It has been observed in the shadowgraph images (c.f. Fig. 20-23 and 24a) that at about the same time when the internal shockwave reflects from the sample, liquid metal is ejected from the sample either in a conically shaped liquid layer or in a stream of

liquid droplets [24-27]. For the present experiments, the penetration depth of laser in metal is very small. Therefore, most of the laser energy is absorbed within a thin layer near the sample surface, which results in a thin molten layer along with a strong evaporation around the laser spot. Consequently, a concave melting pool is formed before the internal shockwave arrives at the sample. As a result, when the internal shockwave strikes the sample surface, the Richtmeyer-Meshkov instability causes the ejected liquid layer to form a conically shaped liquid jet [23]. If the liquid metal is sufficiently thick, the thermal expansion of the liquid results in a convex shape with respect to the sample. As a result, liquid metal will eject in a stream of liquid droplets when the internal shockwave strikes this convex melting pool. Aided by the presence of the vortex ring, the stream of liquid droplets can move in a straight outward trajectory from the sample surface. For example, during laser ablation of silicon with a high energy 266nm laser, the melted layer formed at the silicon surface was transparent to the laser energy when the temperature is close to the critical temperature (~5000K) [20-23]. Consequently, the laser energy can penetrate deeply into the silicon and forms a volumetrically laser heated pool. This is in contrast to laser ablation occurring in most materials which results in a relatively shallow melting pool. As a result, in silicon, the melting pool is convex, and a stream of silicon droplets will be generated when the internal shockwave strikes the convex melting pool. For laser ablation in a vacuum, there is no external shockwave in the background gas, and there is no corresponding internal shockwave in the free expanding vapor plume. Consequently, there is no internal-shockwave-induced melted sample ejection for ablation in a vacuum. Therefore, there is almost no rim (or a very small rim as compared to that in a background gas) around the crater for ablation in vacuum [278].

8. Vortex ring (from tens of ns to ~1μs after the laser pulse, Fig. 11 and 20-23)

Due to the large velocity gradient between the vapor plume and the sample, a boundary layer is generated during the expansion of the vapor plume. This boundary layer is the source of vorticity in the hemispherical flow field. The vorticity is transferred from the region near the sample surface to the whole vapor plume. Due to the slow diffusion transport of vorticity within a few hundreds of ns, the main mechanism for vorticity transfer away from the boundary is convective transport. The vortex region increases immediately after the internal shockwave reaches the sample surface (c.f. Figs. 20-23). The high velocity after the internal shockwave accelerates the transport of the vorticity away from the region near the surface causing the vortex ring to be larger and to be observed in the emission images. The vortex ring distorts the shape of the internal shockwave when coming to the sample surface during the second reflection.

Since the shear stress in the boundary layer is proportional to the relative velocity between the vapor plume and the stationary sample, a faster expansion of the vapor plume corresponding to higher laser energy and/or ablation in a light background gas generates greater shear and a stronger vortex ring. Due to the direction of the vortex, the vortex ring starts to move outward from the laser heated region. For laser ablation in argon and neon for E=10mJ, the weak vortex ring allows the vapor plume always to be hemispherical during the expansion. For ablation in argon and neon with E=30mJ and for ablation in helium with E=10 and 30mJ, stronger vortex rings provide an additional outward velocity for the vapor plume, and the vapor plume no longer retains its hemispherical shape at ~100's ns after the laser pulse. For ablation in helium with E=30mJ, the vapor plume changes to a mushroom shape and then to a spherical (not hemispherical) shape ~200ns after the laser pulse. Because the vortex ring is not included

in the analysis [1], the calculated size then deviates from the measurements. When the laser energy is large and/or the background gas density is small, the presence of the vortex ring causes the high emission region to gradually move to the top of the vapor plume after the laser pulse. The high emission region starts to move back to the sample surface a few μs after the laser pulse when the strength of the vortex ring is reduced by the viscous force resulting from the interaction between the vapor plume and the background gas [29].

Conclusions

The energy conversion efficiency, E, and mass vaporized, M, during laser ablation plasma-plume formation were determined from the comparison of the predicted [5] and measured positions of the external shockwave and contact surface. The quantity of vaporized mass was found to be independent of the ambient gas. However, the laser energy transferred to the ambient scaled inversely with the atomic mass of the gas (He, Ne, and Ar). These results are related to plasma shielding, due to the reflection and absorption of the laser energy by the plasma plume. The time of the onset of plasma shielding with respect to the laser pulse determines the amount of laser energy that arrives at the sample surface, which was similar for ablation in the three gases. Consequently, the molten layer thickness and the amount of sample vaporized were also similar for ablation in the three background gases.

For ablation in a gas with higher atomic mass (e.g. Ar and Ne), the vapor plume expanded more slowly a few ns after the start of the laser pulse, compared to that in a

lower atomic mass (e.g. He). Therefore, the mass density, temperature, and the consequent electron number density of the vapor plume were higher for ablation in Ar and Ne than that in He. This higher electron-number-density vapor plume reflects a significant portion of the incoming laser energy thus reducing the laser energy conversion ratio for ablation in Ar and Ne. In addition, a laser supported detonation (LSD) wave which appeared above the external shockwave could be observed in the shadowgraph images for ablation in Ar and Ne. The high electron number density region followed by the LSD prohibits the laser energy from arriving in the vapor plume, which further reduces the laser energy conversion ratio.

A few 100's of ns after the laser pulse, the simulated value of the vapor plume size deviated from experimentally measured values, when the laser energy was large and/or the background gas density was small. A vortex ring originating near the sample propelled the vapor plume away from the surface. This vortex ring was generated from the boundary layer between the vapor plume and the sample surface; it was not included in the present spherically symmetric analysis. The vortex ring also changed the shape of the internal shockwave at ~100ns after the laser pulse. However, the calculated position of the external shockwave did agree with experiments at all times after the laser pulse for all experimental conditions tested.

According to the present study, experiments requiring higher laser energy conversion efficiency and a larger vapor plume (e.g. laser induced breakdown spectroscopy) should be conducted in a lower atomic mass gas. However, the vapor plume does not stay in contact with the sample surface and does not retain its hemispherical shape shortly after the laser pulse. For ablation in a higher atomic mass

background gas, even though the laser energy conversion efficiency is reduced, the vapor plume retains a hemispherical shape and stays in contact with the sample surface for a longer time during the laser ablation; this benefits applications requiring a stable vapor plume (e.g. a laser plasma lens).

Acknowledgement

This work was supported by the U.S. Department of Energy, Office of Basic Energy Sciences, Chemical Sciences Division at the Lawrence Berkeley National Laboratory under contract number DE-AC02-05CH11231. The authors are pleased to acknowledge the helpful discussions with Howard Baum of NIST and Paul Berdahl of LBNL.

Reference

[1] I. Horn, M. Guillong, and D. Gunther, Applied Surface Science **182**(1-2), 91 (2001).

[2] A. Bogaerts A, Chen Z., Gijbels R., and Vertes A, Spectrochimica Acta Part B 58, 1867 (2003).

[3] G. Callies, P. Berger, and H. Hugel, Journal of Physics D-Applied Physics **28**(4), 794 (1995).

[4] R. G. Root, in Laser-induced plasmas and applications , edited by L. J. Radziemski and D. A. Cremers (Marcel Dekker Inc., New York, 1989).

[5] S. B. Wen, X. Mao, R. Greif, and R. E. Russo, Study of the expansion of the vapor

plume generated by laser ablation with a background gas – Part A. Theoretical Analysis (submitted).

[6] P. G. Saffman, Vortex Dynamics (Cambridge University Press, 1995)

[7] E. M. Lifshitz and L. D. Landau, Fluid Mechanics, 2nd edition (Butterworh-Heinemann, 1987).

[8] A. Vertes, R. Gijbels, and F. Adams, Laser Ionization Mass Analysis, (John Wiley & Son, New York, 1993).

[9] M. Von Allmen, Laser-beam interactions with materials (Springer-Verlag, Berlin, 1987)

[10] J. J. Chang and B. E. Warner, Applied Physics Letters **69**(4), 473 (1996).

[11] Z. Y. Zhang and G. Gogos, Physical Review B **69**(23), 235403 (2004)

[12] A. Sollier, L. Berthe, and R. Fabbro, European Physical Journal-Applied Physics **16**(2), 131 (2001).

[13] N. Arnold, J. Gruber, and J. Heitz, Applied Physics A-Materials Science & Processing **69**, S87-S93 (1999).

[14] C. Boulmer-Leborgne, J. Hermann, and B. Dubreuil, Plasma Sources Science and Technology 2, 219 (1993).

[15] X. Mao, S. B. Wen, and R. E. Russo, Time Resolved Laser-Induced Plasma Dynamics (submitted).

[16] J. D. Anderson, Modern Compressible flow with historical perspective, 3rd edition, (Mc Graw Hill, New York, 2002)

[17] D. C. Hamilton, D. J. James, and S. A. Ramsden, Journal of Physics D-Applied Physics **10**(7), 1011 (1977).

[18] L. A. Bolshov, V. A. Vorobyev, M. F. Kanevsky, and S. Y. Chernov, Izvestiya Akademii Nauk Sssr Seriya Fizicheskaya **55**(7), 1305 (1991).

[19] P. E. Nielsen and G. H. Canavan, in Laser interaction and related plasma phenomena, Volume 3A, edited by H. J. Schwarz and H. Hora (Plenum, New York, 1974).

[20] H. Reinholz, G. Ropke, I. Morozov, V. Mintsev, Y. Zaparoghets, V. Fortov, and A. Wierling, Journal of Physics A-Mathematical and General **36**(22), 5991 (2003).

[21] Y. B. Zel'dovich and Yu. P. Raizer, in *Physics of Shock Waves and High-Temperature Hydrodynamic Phenomena*, edited by W. D. Hayes and R. F. Probstein (Academic, London, 1966).

[22] L. I. Sedov, Similarity and Dimensional Methods in Mechanics, 10th edition (CRC press, Ann Arbor, 1993).

[23] M. Brouillette, Annual Review of Fluid Mechanics **34**, 445 (2002).

[24] C. Liu, Ph. D thesis, University of California at Berkeley, 2005.

[25] J. H. Yoo, S. H. Jeong, X. L. Mao, R. Greif, and R. E. Russo, Applied Physics

Letters **76**(6), 783 (2000).

[26] S. B. Wen, X. Mao, C. Liu, R. Greif, and R. E. Russo, Wen S B, Mao X L, Liu C, Greif R, and Russo R. E, 8th International conference on laser ablation, Banff, Canada, 2005.

[27] R. V. Karapetyan and A. A. Samokhin, Soviet Journal of Quantum Electronics 4(9), 1141 (1975).

[28] X. L. Mao, W. T. Chan, M. A. Shannon, and R. E. Russo, Journal of Applied Physics **74**(8), 4915 (1993).

[29] S. B. Wen, X. L. Mao, R. Greif, and R. F. Russo, Journal of Applied Physics **100**(5), 053104 (2006).

Nomenclature

E_{ion}	Ionization potential
e	Electron charge
k	Boltzmann constant
R_c	Position of the contact surface
R_e	Position of the external shockwave front
$\dot{R}_c$	Velocity of the contact surface
$\dot{R}_e$	Velocity of the external shockwave front
M_e	Compressed air mass in the external shockwave region
P_e	Momentum in the external shockwave region

γ_p	Specific heat ratio of the plume
c_p	Specific heat with constant pressure
c_v	Specific heat with constant volume
h_{lv}	Latent heat of vaporization
k_B	Boltzmann constant
m_e	Electron mass
n	Refractive index of the background gas
n_{ec}	Critical electron number density
p_s	Saturation pressure at surface temperature T_s
p_0	Vapor pressure at the sample surface T_s
p_e	Pressure after the external shockwave
$Q_{ab,laser}$	Rate of absorption of the laser energy in the solid phase region
$Q_{ab,v,laser}$	Rate of absorption of the laser energy in the gas phase region
R	Gas constant
ρ_e	Density after the external shockwave
ρ_0	Density at the sample surface temperature T_s
u_e	Velocity after the external shockwave
v_0	Vaporization velocity at the sample surface
T	Temperature
T_b	Boiling temperature
T_e	Temperature after the external shockwave
T_g	Temperature of the background air
T_s	Surface temperature
s	Factor that accounts for the recondensation at the sample surface
ε_0	free space permittivity
ρ	Density
ρ_g	Background air density
λ	Laser wavelength
γ_g	Specific heat ratio of the background air
ω	Laser frequency
$\Re_p$	Gas constant of vapor plume
K	Heat conductivity
$\Re_g$	Gas constant of background air
C_1	Constant
E_{ext}	Energy driving the external shockwave
m	Molecular mass of vapor,

n_{ec}	Critical electron density

List of Figures

Figure 7. Shadowgraph images of the laser ablation in neon with E=10mJ (From 0-30ns). Shockwave and vapor plume can be observed from ~3ns after the beginning of the laser pulse. No LSD was observed. LSC was observed from ~10ns after the beginning of the laser pulse.

Figure 8. Shadowgraph images of the laser ablation in helium with E=10mJ (From 0-30ns). Shockwave and vapor plume can be observed from ~3ns after the beginning of the laser pulse. No LSD was observed. LSC was observed from ~12ns after the beginning of the laser pulse.

Figure 9. Shadowgraph images of the laser ablation in argon with E=30mJ (From 0-30ns). Shockwave and vapor plume can be observed from ~2ns after the beginning of the laser pulse. LSC was observed from 4 to 9ns after the beginning of the laser pulse. LSC was observed from ~12ns after the beginning of the laser pulse.

Figure 10. Shadowgraph images of the laser ablation in neon with E=30mJ (From 0-30ns). Shockwave and vapor plume can be observed from ~2ns after the beginning of the laser pulse. LSC was observed from 4 to 7ns after the beginning of the laser pulse. LSC was observed from ~12ns after the beginning of the laser pulse.

Figure 11. Shadowgraph images of the laser ablation in helium with E=30mJ (From 0-30ns). Shockwave and vapor plume can be observed from ~2ns after the beginning of the laser pulse. No LSD was observed. LSC was observed from ~10ns after the beginning of the laser pulse.

Figure 12. Line emission images of the laser ablation in helium with E=10mJ. Internal shockwave struck the sample at ~10ns after the beginning of the laser pulse. A vortex ring can be observed ~400ns after the laser pulse.

Figure 13. Line emission images of the laser ablation in helium with E=30mJ. Internal shockwave struck the sample at ~12ns after the beginning of the laser pulse. A vortex ring can be observed ~200ns after the laser pulse.

Figure 14. Line emission images of the laser ablation in argon with E=10mJ. Internal shockwave struck the sample at ~12ns after the beginning of the laser pulse. No vortex ring was observed.

Figure 15. Line emission images of the laser ablation in argon with E=30mJ. Internal shockwave struck the sample at ~13ns after the beginning of the laser pulse. A vortex ring can be observed ~500ns after the laser pulse.

Figure 16. The liquid sample ejection and LSC in shadowgraph images (a) 10ns after laser pulse in helium for E=30mJ (b) 20ns after laser pulse in helium for E=30mJ. The liquid sample ejection can be observed at the bottom of the vapor plume after the internal shockwave strikes the sample surface (~7ns in He for E=30mJ from plume emission

images). The ejected liquid sample is then evaporated by the high temperature plasma. The LSC can be observed at the tip of the vapor plume ~10ns to ~20ns after the end of laser pulse in three background gases.

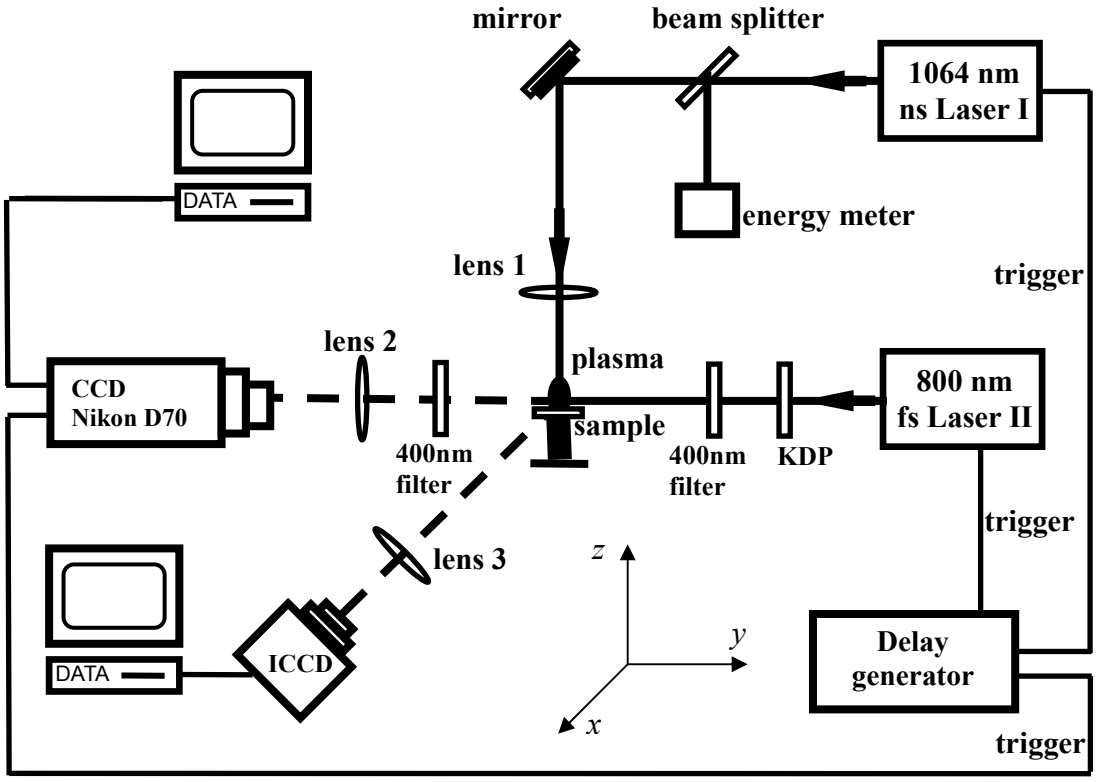
mirror
beam splitter
1064 nm
ns Laser I
DATA
energy meter
lens 1
trigger
lens 2
plasma
CCD
Nikon D70
800 nm
fs Laser II
sample
400nm
filter
400nm
filter
KDP
trigger
lens 3
z
y
x
DATA
ICCD
Delay
generator
trigger

Figure 1

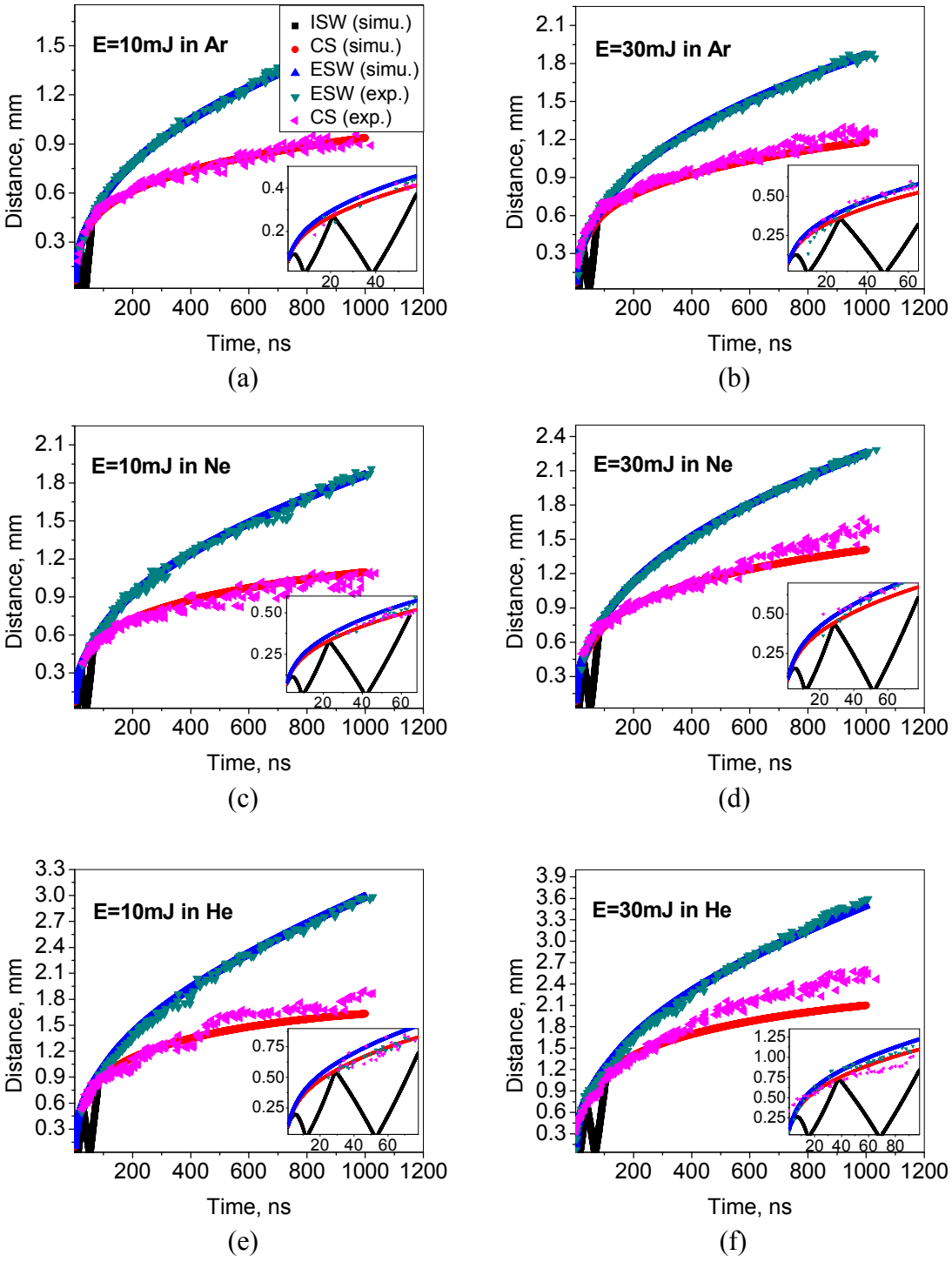
E=10mJ in Ar
ISW (simu.)
CS (simu.)
ESW (simu.)
ESW (exp.)
CS (exp.)
Distance, mm
Time, ns
(a)
E=30mJ in Ar
Distance, mm
Time, ns
(b)
E=10mJ in Ne
Distance, mm
Time, ns
(c)
E=30mJ in Ne
Distance, mm
Time, ns
(d)
E=10mJ in He
Distance, mm
Time, ns
(e)
E=30mJ in He
Distance, mm
Time, ns
(f)

Figure 2

Laser energy (E) at 10mJ (fluence $\approx 14 J/cm^2$)

Ambient gas	Ar (μm^3)	Ne (μm^3)	He (μm^3)
Down volume	165,000	170,000	180,000

Laser energy (E) at 30mJ (fluence $\approx 42 J/cm^2$)

Ambient gas	Ar (μm^3)	Ne (μm^3)	He (μm^3)
Down volume	480,000	475,000	460,000

(a)

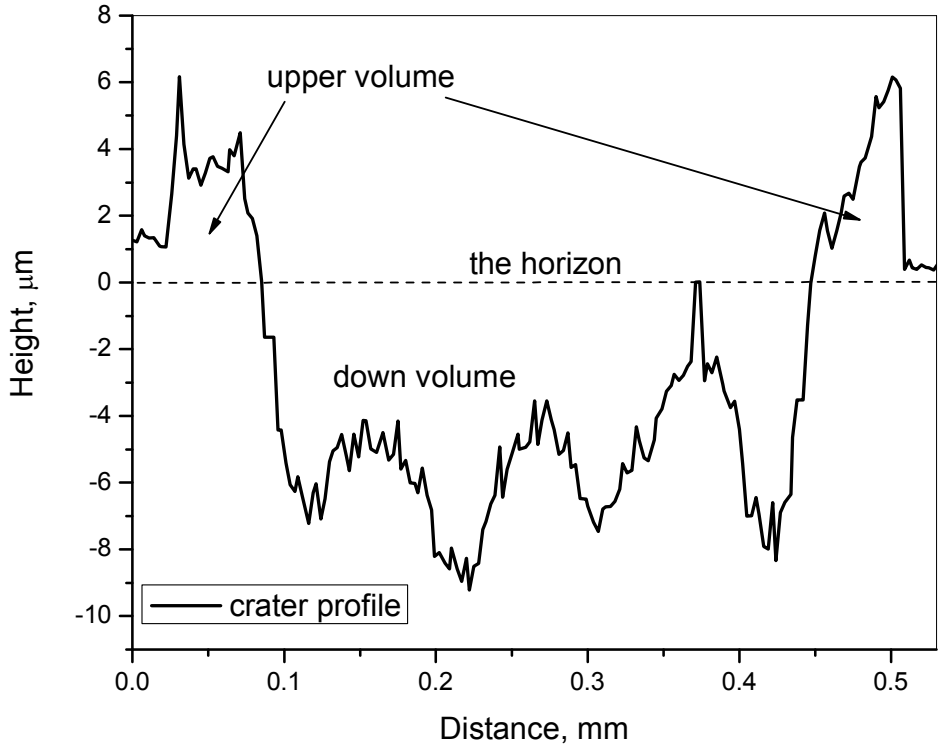

(b)

Figure 3

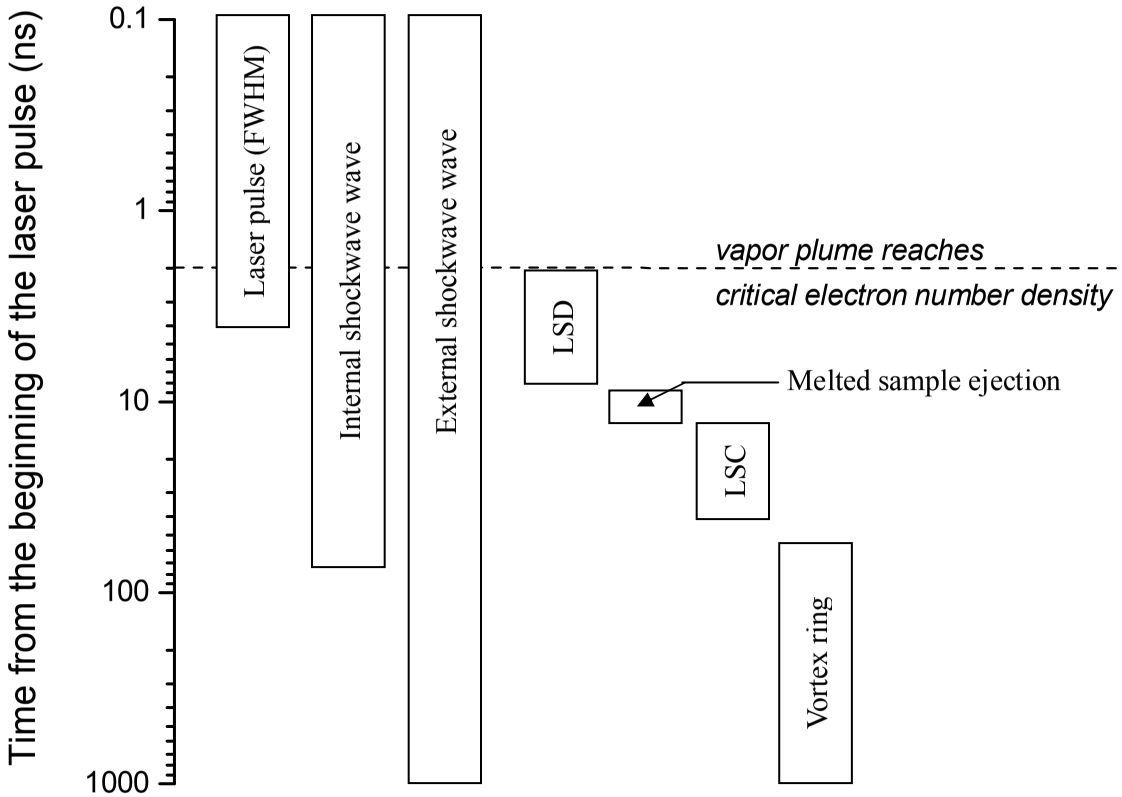
Time from the beginning of the laser pulse (ns)
0.1
1
10
100
1000
Laser pulse (FWHM)
Internal shockwave wave
External shockwave wave
LSD
Melted sample ejection
LSC
Vortex ring
vapor plume reaches
critical electron number density

Figure 4

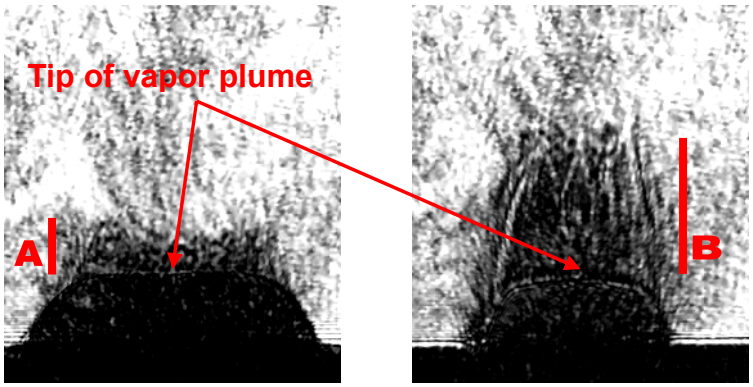
Tip of vapor plume
A
B

(a) (b)

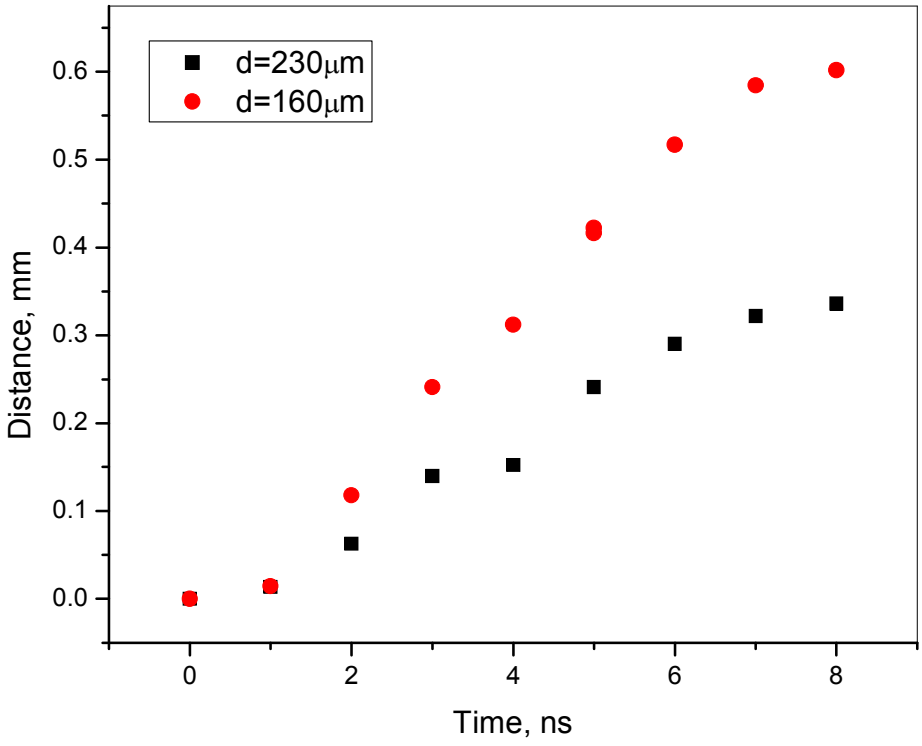
d=230μm
d=160μm
Distance, mm
Time, ns
0.0
0.1
0.2
0.3
0.4
0.5
0.6
0
2
4
6
8

(c)

Figure 5

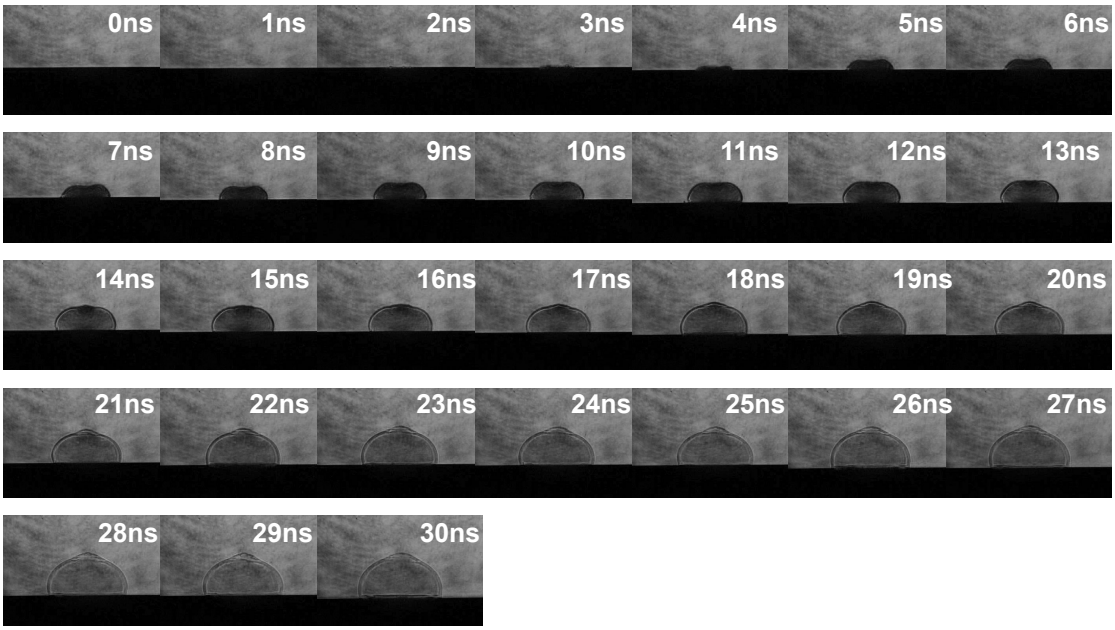

Figure 6

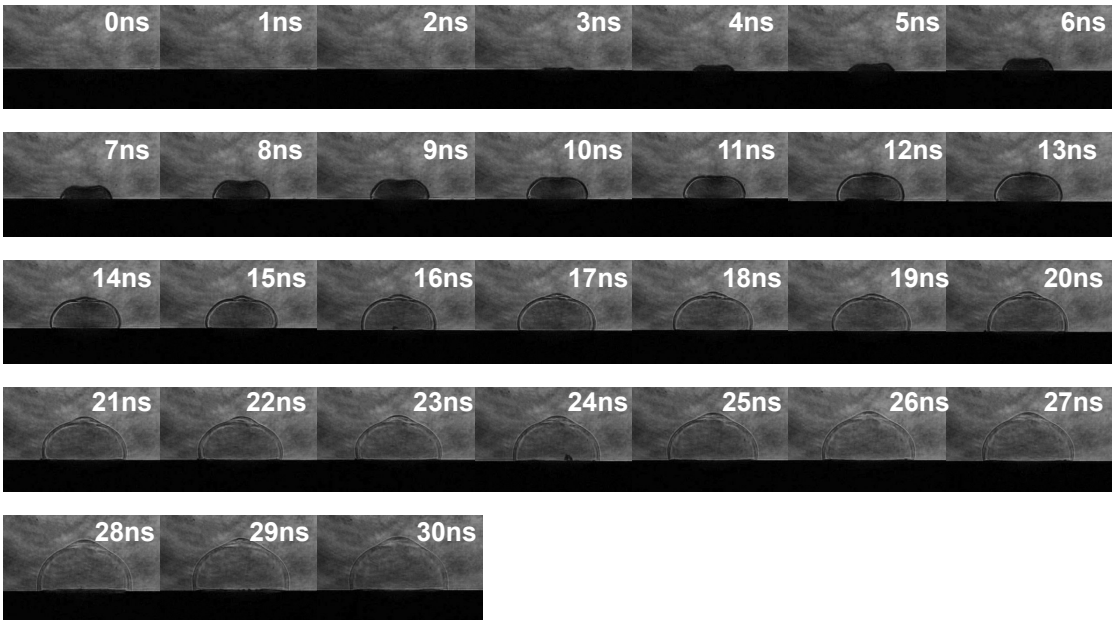

Figure 7

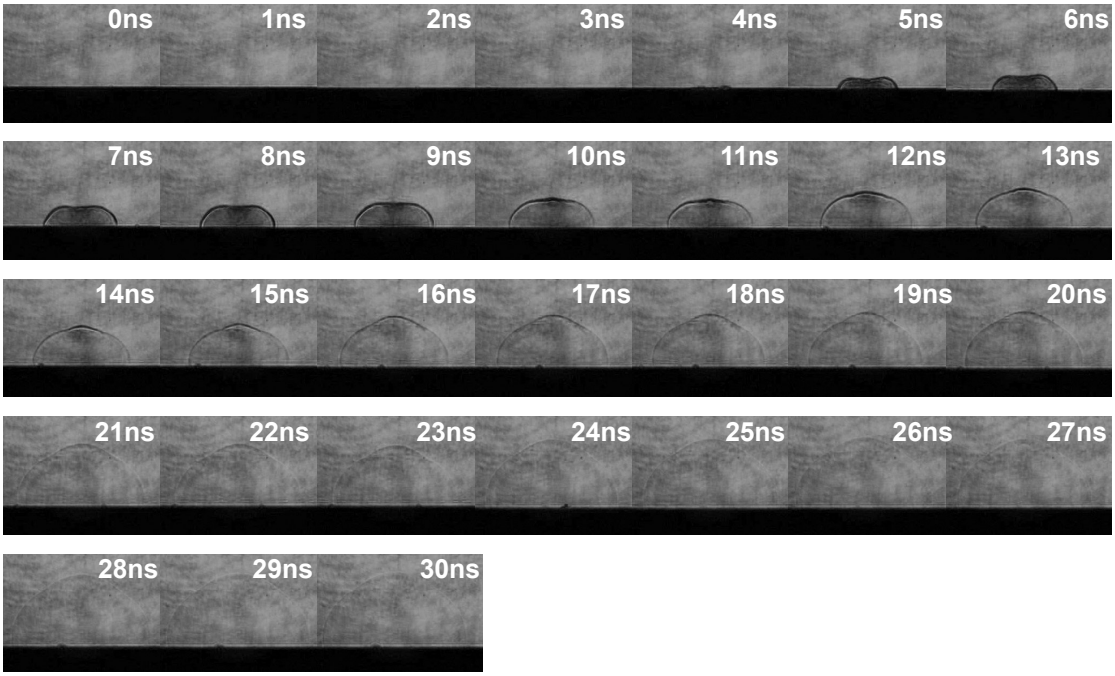

Figure 8

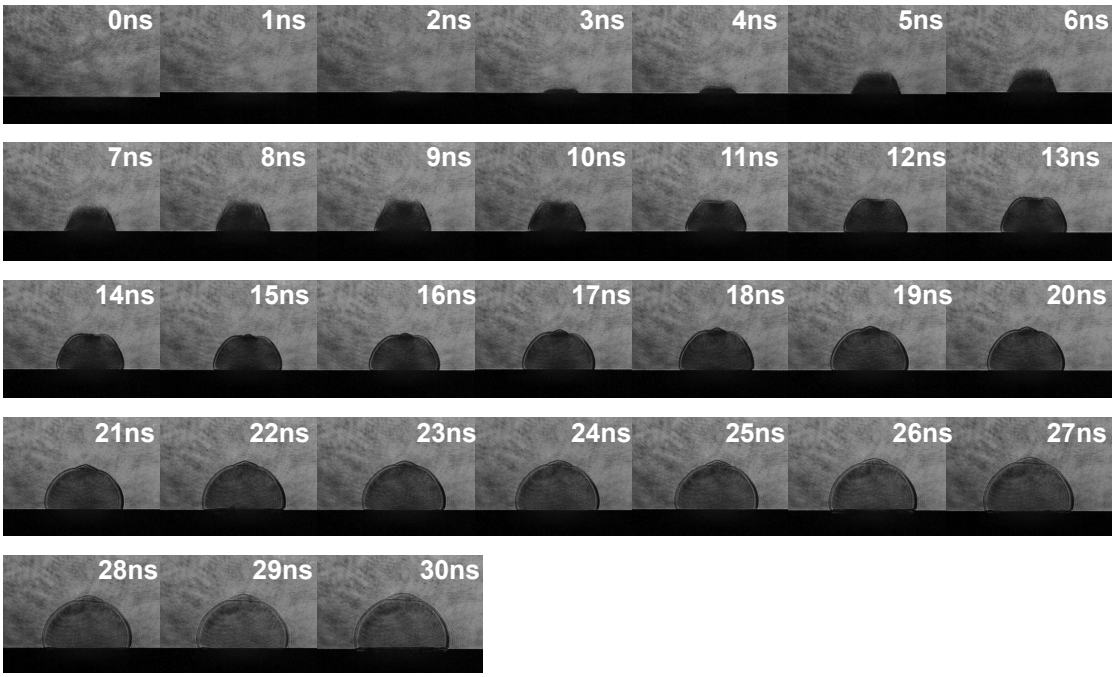

Figure 9

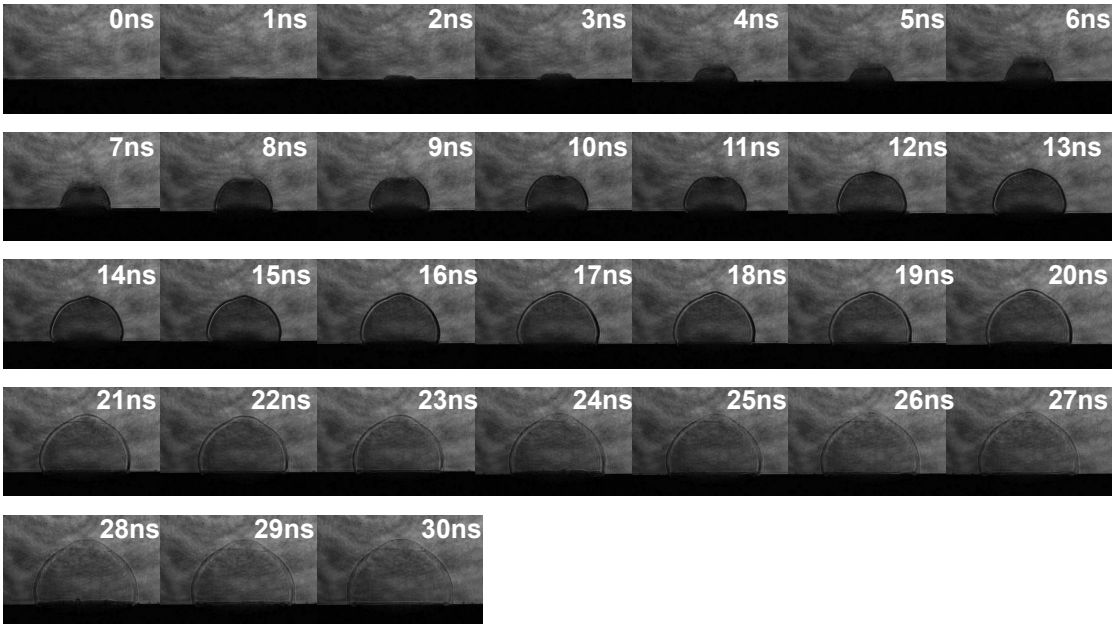

Figure 10

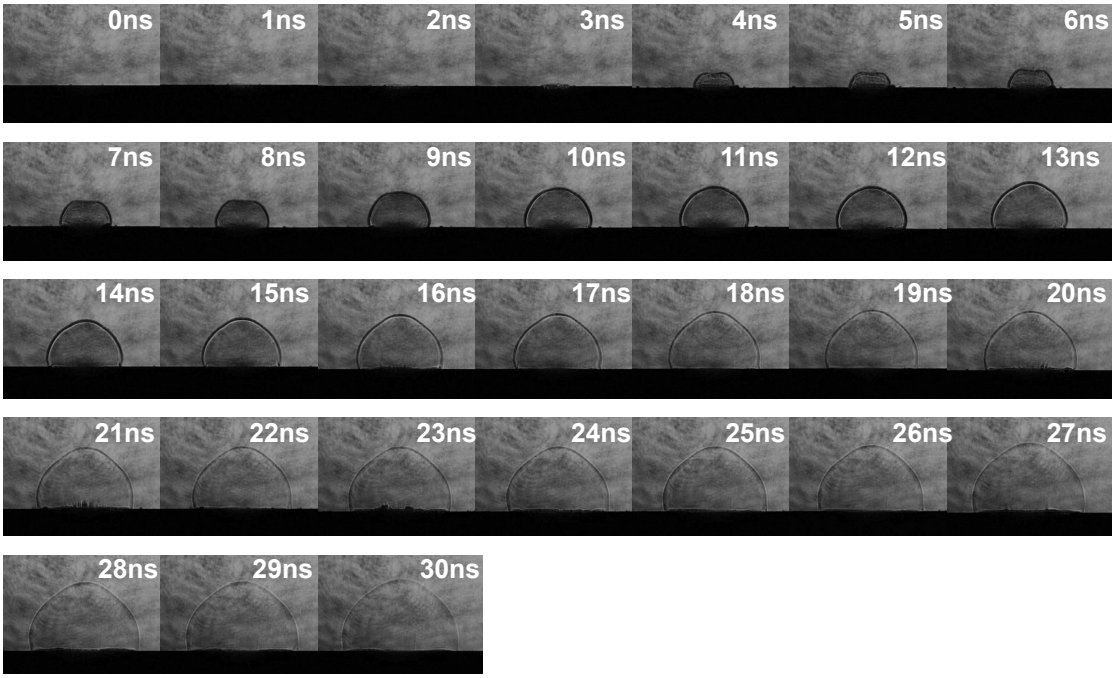

Figure 11

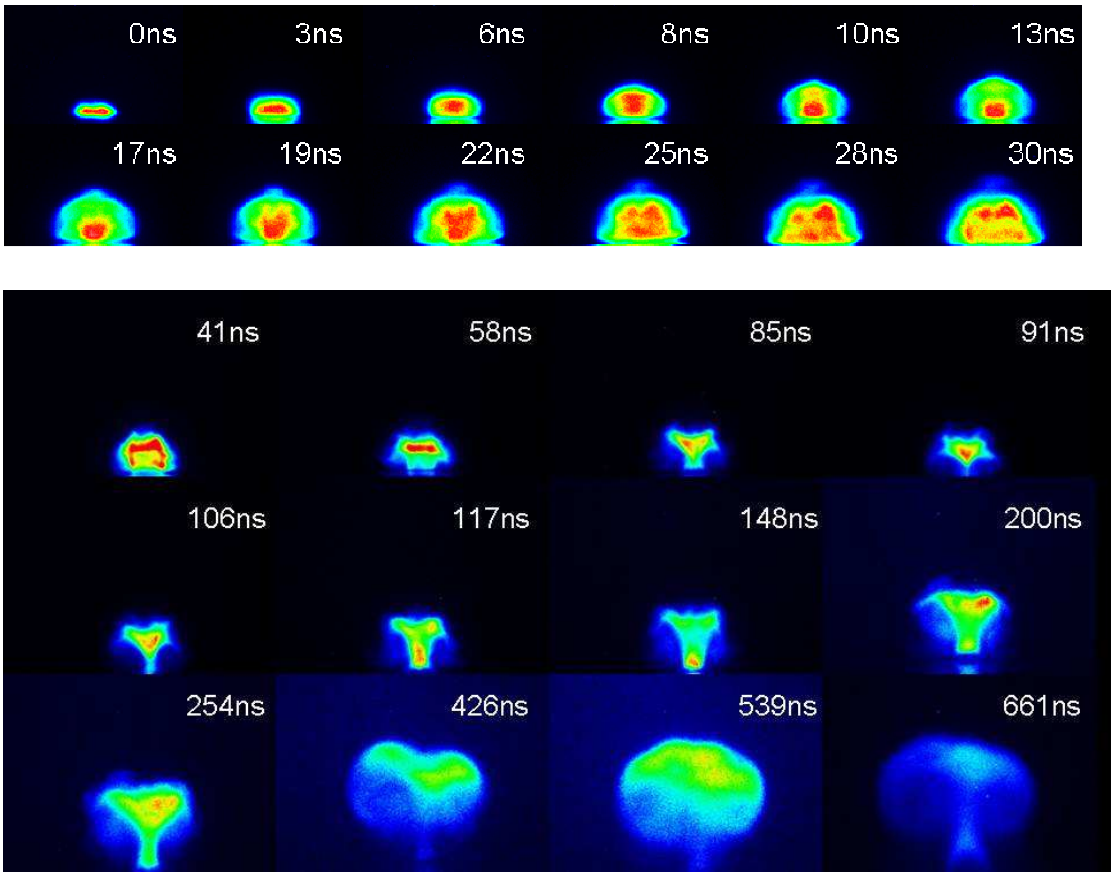
0ns
3ns
6ns
8ns
10ns
13ns
17ns
19ns
22ns
25ns
28ns
30ns
41ns
58ns
85ns
91ns
106ns
117ns
148ns
200ns
254ns
426ns
539ns
661ns

Figure 12

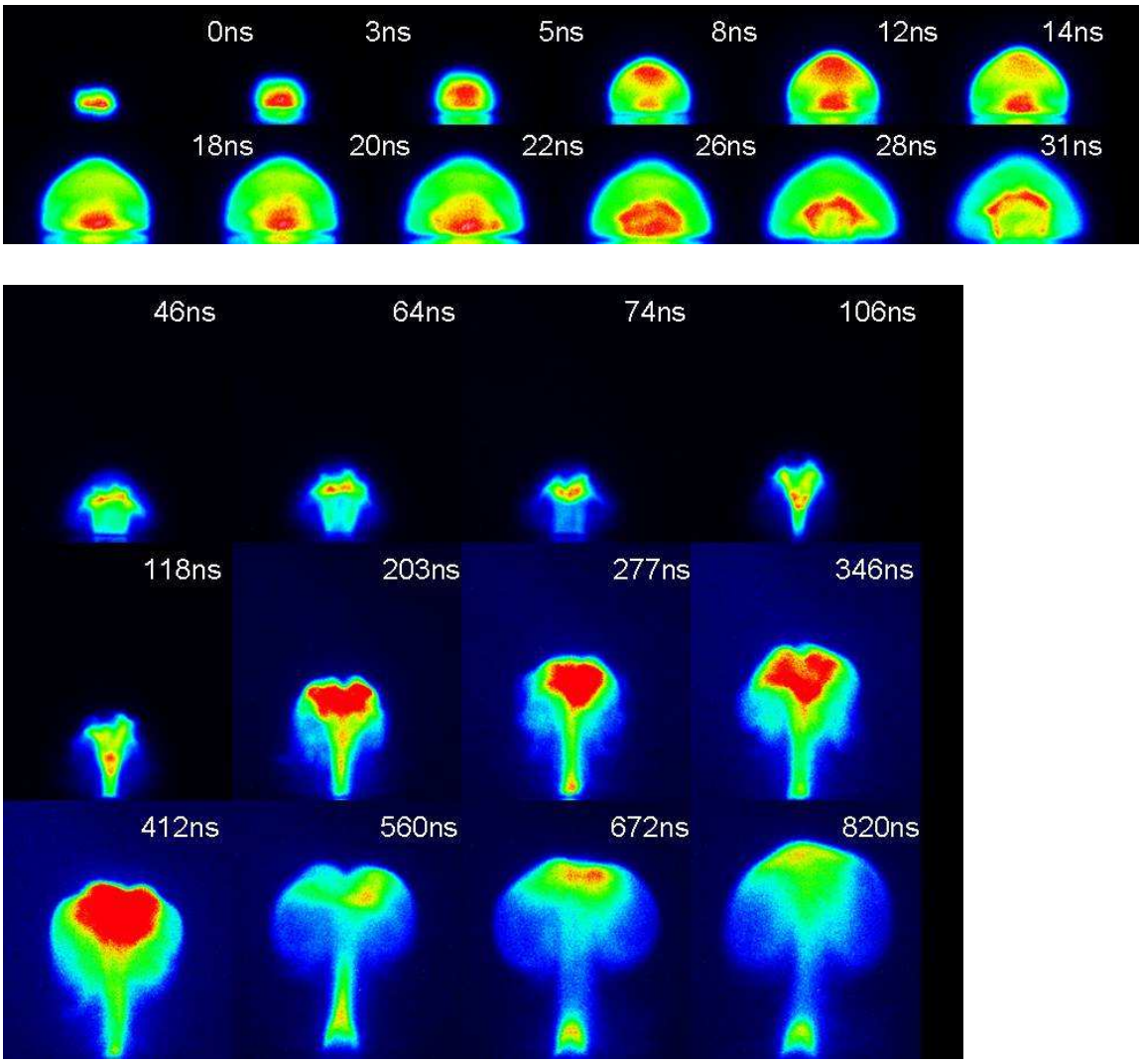
0ns
3ns
5ns
8ns
12ns
14ns
18ns
20ns
22ns
26ns
28ns
31ns
46ns
64ns
74ns
106ns
118ns
203ns
277ns
346ns
412ns
560ns
672ns
820ns

Figure 13

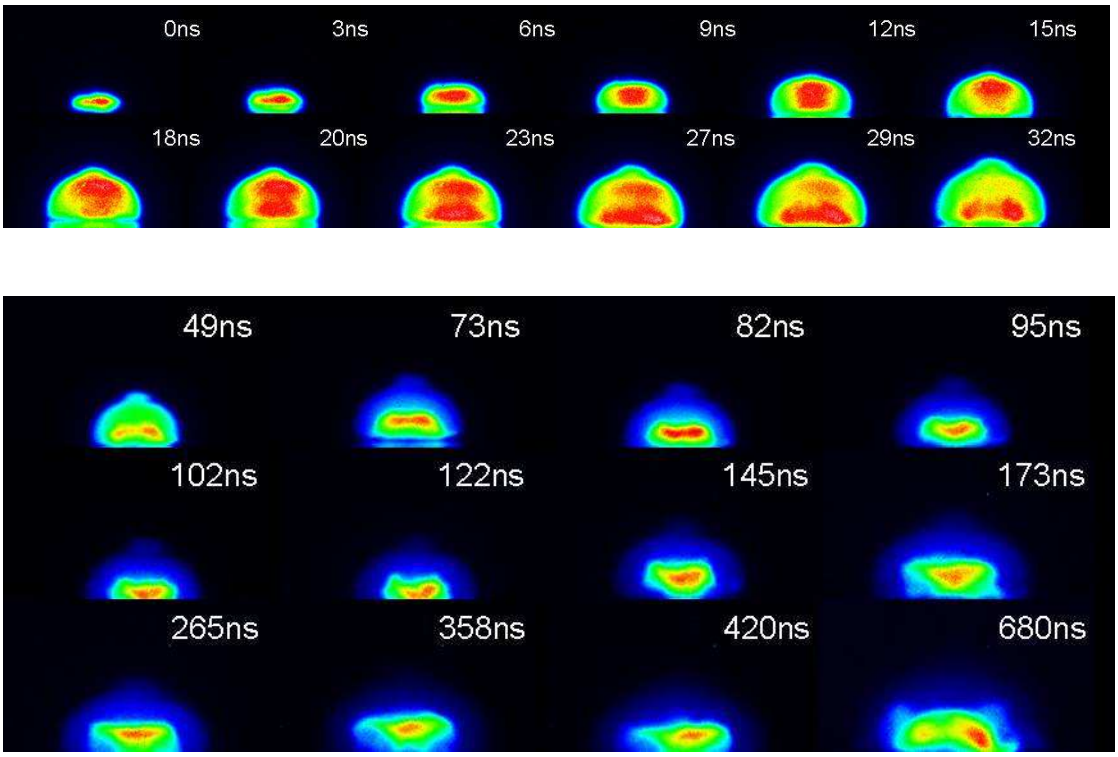
0ns
3ns
6ns
9ns
12ns
15ns
18ns
20ns
23ns
27ns
29ns
32ns

49ns
73ns
82ns
95ns
102ns
122ns
145ns
173ns
265ns
358ns
420ns
680ns

Figure 14

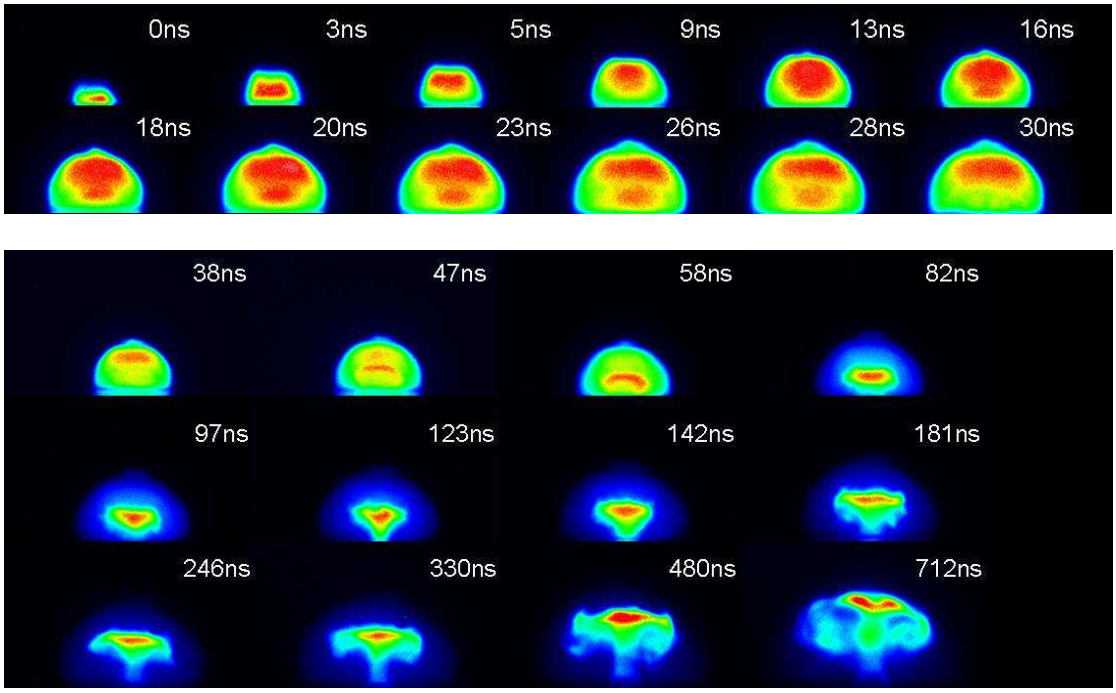
0ns
3ns
5ns
9ns
13ns
16ns
18ns
20ns
23ns
26ns
28ns
30ns
38ns
47ns
58ns
82ns
97ns
123ns
142ns
181ns
246ns
330ns
480ns
712ns

Figure 15

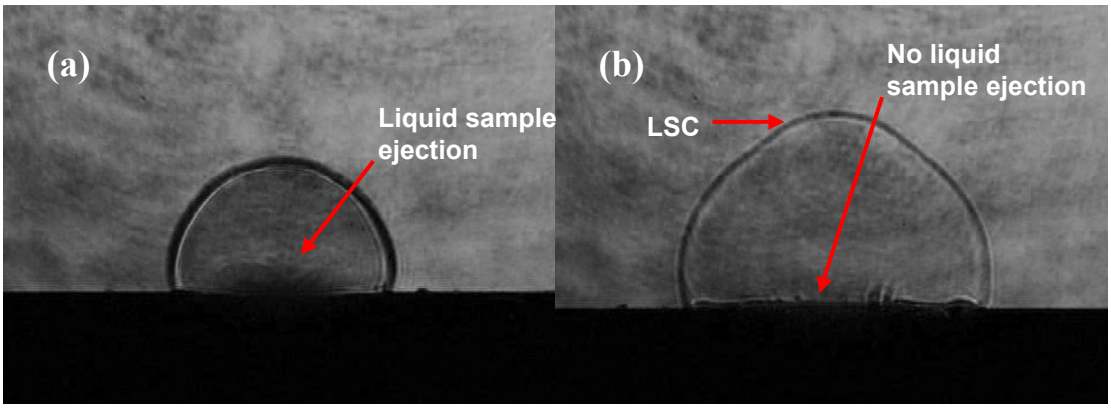

Figure 16